Combining Observations from Multiple Platforms across the Kuroshio Northeast of Luzon: A Highlight on PIES Data

VIGAN MENSAH

Institute of Oceanography, National Taiwan University, Taipei, Taiwan

MAGDALENA ANDRES

Woods Hole Oceanographic Institution, Woods Hole, Massachusetts

REN-CHIEH LIEN, BARRY MA, AND CRAIG M. LEE

Applied Physics Laboratory, University of Washington, Seattle, Washington

SEN JAN

Institute of Oceanography, National Taiwan University, Taipei, Taiwan

ABSTRACT

This study presents amended procedures to process and map data collected by pressure-sensor-equipped inverted echo sounders (PIESs) in western boundary current regions. The modifications to the existing methodology, applied to observations of the Kuroshio from a PIES array deployed northeast of Luzon, Philippines, consist of substituting a hydrography-based mean travel time field for the PIES-based mean field and using two distinct gravest empirical mode (GEM) lookup tables across the front that separate water masses of South China Sea and North Pacific origin. In addition, this study presents a method to use time-mean velocities from acoustic Doppler current profilers (ADCPs) to reference (or "level") the PIES-recorded pressures in order to obtain time series of absolute geostrophic velocity. Results derived from the PIES observations processed with the hydrography-based mean field and two GEMs are compared with hydrographic profiles sampled by Seagliders during the PIES observation period and with current velocity measured concurrently by a collocated ADCP array. The updated processing scheme leads to a 41% error decrease in the determination of the thermocline depth across the current, a 22% error decrease in baroclinic current velocity shear, and a 61% error decrease in baroclinic volume transports. The absolute volume transport time series derived from the leveled PIES array compares well with that obtained directly from the ADCPs with a root-mean-square difference of 3.0 Sv ($1 \text{ Sv} \equiv 10^6 \text{ m}^3 \text{ s}^{-1}$), which is mainly attributed to the influence of ageostrophic processes on the ADCP-measured velocities that cannot be calculated from the PIES observations.

1. Introduction

The inverted echo sounder (IES) and pressure-sensor-equipped inverted echo sounder (PIES) have been used for nearly three decades for studies of the thermocline depth (e.g., Watts and Rossby 1977) and geostrophic currents and transports (e.g., Book et al. 2002), and are

particularly well suited for studies of western boundary currents. A PIES sits on the seabed and measures the time-varying pressure and the time-varying round-trip time (τ) for an acoustic pulse to travel between the instrument and the sea surface. In many regions—because of the dependence of sound speed on temperature, salinity, and pressure—there is a strong relationship between τ and the vertical structure of hydrographic properties; therefore, τ can be used to infer profiles of temperature and specific volume anomaly through the use of gravest empirical mode (GEM) lookup tables (Meinen and Watts 2000; Sun and Watts 2001; Watts

Corresponding author address: Sen Jan, Institute of Oceanography, National Taiwan University, No. 1, Sect. 4, Roosevelt Rd., Taipei 10617, Taiwan.
E-mail: senjan@ntu.edu.tw

et al. 2001). Subsequently, profiles of geostrophic velocity shear and relative geostrophic volume transport between pairs of instruments can be calculated with the thermal wind equations. Using the time-varying pressure differences between instruments, these relative shears and transports can be made absolute after a process called "leveling" via a suitable reference velocity, typically measured by a near-bottom current meter just above the benthic boundary layer (e.g., Andres et al. 2008; Donohue et al. 2010).

The τ data may be mapped between instrument sites using an objective mapping method (e.g., Donohue et al. 2010 derived from Bretherton et al. 1976). However, errors associated with the GEM lookup table, τ measurement and processing steps, and this mapping procedure may each influence the full-depth hydrographic profiles derived from τ. Consequently, the PIES data–derived horizontal density gradients and vertical shears of the horizontal currents contain errors. These in turn propagate to errors in the current velocity magnitude, structure, and volume transports estimates. The procedures presented in the following are developed to minimize these errors.

As part of a joint U.S.–Taiwan study to observe the variability of the western boundary current in the western North Pacific, the Kuroshio, three types of instruments were deployed from June 2012 to June 2013 to measure the hydrographic properties and current velocities northeast of Luzon, Philippines. The concurrent measurements carried out by PIESs, Seagliders, and acoustic Doppler current profilers (ADCPs) along 18.75°N provide a unique opportunity to compare the PIES-derived results with those directly measured by the other instruments. The comparison motivates the improved processing and mapping techniques described here. The techniques are useful, since the study region presents several challenges for the use of PIESs to establish the Kuroshio's mean and time-varying velocity structure and transport: a large bathymetric slope across the mooring array, sparse historical hydrographic data, and the presence of different water masses of South China Sea and North Pacific origin in the study region. Since some of these characteristics are common to other regions along the Kuroshio path from the Philippines to south of Japan, the techniques derived here have wider applicability beyond the array east of Luzon. Furthermore, this study demonstrates the benefit of combining multiple observational platforms in a field program to leverage the different data types.

In this study, we build on the methodology of Donohue et al. (2010) and adapt this to achieve improved accuracy in the estimates of time-varying density structure and baroclinic velocities (and baroclinic transports) derived from the PIES τ data east of Luzon. We also obtain estimated absolute velocities (and absolute transports) from the PIES τ and pressure data by modifying the leveling method (Andres et al. 2008; Donohue et al. 2010) to use velocities from upper-ocean upward-looking ADCPs instead of velocities from near-bottom current meters. We evaluate the original and amended processing schemes by comparing the PIES-derived quantities (hydrographic structure, velocity profiles, and volume transports) with those derived from the Seaglider and ADCP data (i.e., "reference measurements"). A description of the PIES original and amended processing procedures is provided in section 2. Section 3 compares PIES data with the reference measurements. Section 4 discusses the effects of the amended procedures and the discrepancies between the PIES and reference data. A summary and conclusions are provided in section 5.

2. Data and methodology

a. Data collection

The instruments deployed as part of the joint U.S.–Taiwan research projects Origins of the Kuroshio and Mindanao Current (OKMC) and Observations of Kuroshio Transports and Variabilities (OKTV) consisted of an array of PIESs, an array of ADCP moorings, and Seaglider transects northeast of Luzon along 18.75°N to obtain continuous observations of the Kuroshio near its origin. The ADCP array included six subsurface moorings (M line) spanning 80 km between 122.10° and 122.87°E with moorings separated by ~16 km (yellow squares in Fig. 1). The moorings were deployed from June 2012 to June 2013 and each one, M1–M6, included an upward-looking 75-kHz ADCP at ~450-m depth that measured horizontal velocities to within 50 m of the sea surface. The instruments sampled every 90 s, and the data were averaged into 15-min ensembles in 8-m vertical bins. These ADCPs directly measured the time-varying Kuroshio velocities in this region for the first time (Lien et al. 2014).

Concurrently, about 7 km farther north, along 18.81°N, four PIESs (H1–H4) were deployed across the Kuroshio between 122.00° and 123.00°E, at about 30-km spacing, and a fifth instrument (H5) was moored at 19.10°N, 122.58°E, ~30 km downstream of the main line of PIESs (green triangles in Fig. 1). The PIESs recorded τ and pressure every 10 min and data were processed to provide hourly measurements (Kennelly et al. 2007). The τ measurements at H3 were noisy and are therefore not analyzed here, though the pressure record from this site is of good quality and is included in the analysis.
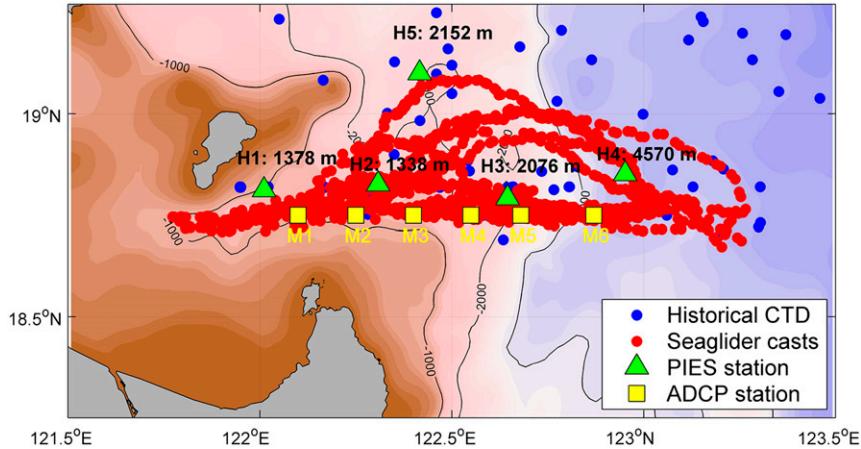
FIG. 1. PIES and ADCP arrays northeast of Luzon; Seaglider dives and historical casts used for building the GEM lookup table and the Seaglider-based mean τ field.

During the 7-month period from November 2012 to May 2013, two Seagliders measured continuously temperature and salinity profiles, nominally along 18.75°N, between 121.8° and 123.2°E. The gliders were equipped with a CTD and sampled every 8 s, completing a profile from the surface to a maximum depth of 1000 m, four to five times a day. The resulting horizontal and vertical resolutions were ~5–10 km and ~5 m, respectively. Figure 1 also shows the locations of the Seaglider dives (red bullets).

b. Standard processing to obtain relative velocity profiles

1) PROCESSING ROUTINE

The first step of PIES processing is to develop the region's GEM lookup tables. The GEM is typically built using all hydrographic profiles available near a study area. A synthetic τ between the sea surface and a reference pressure level is calculated for each of these profiles as

$$\tau_{index} = 2 \int_{p_{index}}^{0} \frac{1}{g\rho(S,T,P)c(S,T,P)} dP, \qquad (1)$$

where ρ and c are the water density and the sound speed in seawater, respectively, as functions of temperature T, salinity S, and pressure P; g is the gravitational acceleration; and p_{index} is the reference level below which the variance of the hydrographic properties is low.

For the PIES array east of Luzon, a total of 1590 Seaglider profiles and 117 historical CTD and Argo float profiles (blue bullets in Fig. 1) acquired within 18.67°–19.25°N, 121.67°–123.5°E are used to build the GEM. The reference level, which is set to 800 dbar (i.e., $\tau_{index} = \tau_{800}$)

to include a high number of hydrographic profiles, is well below the region's pycnocline, ~300-m depth (Tsai et al. 2015). A cubic spline relation between synthetic τ_{index} [calculated from each cast's hydrographic data and Eq. (1)] and observed temperature is fitted, separately, at levels from the surface to 4000 dbar and at 10-dbar intervals, establishing the lookup table between τ_{800} and the vertical profiles of temperature (Meinen and Watts 2000). The same operation is repeated for the specific volume anomaly, whose profiles were previously calculated from the measured pressure, temperature, and salinity.

The method routinely employed to process PIESs' τ data so they can be used with these lookup tables (e.g., Donohue et al. 2010) includes 1) subtracting the nonsteric contribution of the tide from the measured travel time; 2) converting the τ measured at the instrument's level to the reference level used in the GEM, τ_{index}; 3) removing a residual τ generated by the variations of the seasonal thermocline (Tracey and Watts 1986; Watts et al. 2001); and 4) calculating daily averages of τ_{index} for each PIES site. Each daily-averaged τ_{index} is subsequently mapped through an optimal interpolation scheme derived from Bretherton et al. (1976).

Northeast of Luzon the spacing between adjacent PIESs is about 30–40 km, and 10 km is chosen here as the horizontal scale for gridding τ_{index}. The gridding process is carried out iteratively, with separate mappings for a mean field and a residual field, with the latter based on empirically determined correlation length scales (Andres et al. 2008; Donohue et al. 2010). The two fields are added to provide the final time-varying mapped fields. The time-varying mapped τ_{index} is then converted through the GEM to full-depth hydrographic profiles, yielding daily cross sections of specific volume anomaly

and temperature profiles at 10-km resolution across the Kuroshio. Subsequently, the specific volume anomaly at each grid cell is vertically integrated to calculate the baroclinic velocity relative to the reference level (e.g., 800 dbar) using

$$V_{\text{BC}}(P_z, x_n) = \frac{\int_{P_{\text{bot}}}^{P_z} \delta(x_{n+3}) \, dP - \int_{P_{\text{bot}}}^{P_z} \delta(x_{n-3}) \, dP}{fL}, \quad (2)$$

where P_z is the pressure at any given depth z (P_{bot} being the bottom pressure), δ is the specific volume anomaly, L is the distance between the grid cell at x_{n+3} and x_{n-3}, (n is the gridcell zonal index for the 10-km-spaced grid), f is the Coriolis parameter, and $dP = 1$ dbar.

2) ERROR SOURCES IN THE STANDARD PROCESS

For PIESs deployed in the Kuroshio Extension region east of Japan, the combined errors associated with the τ processing were found to yield an uncertainty of ~1 ms (Donohue et al. 2010), and the conversion from τ measured by an instrument to τ_{index} accounted for the largest source of this uncertainty (0.7 ms). The standard procedure for the conversion involves finding a relationship between the τ at the depth of a given instrument $\tau_{\text{instrument}}$ and the τ_{index}. This relationship is often, but not necessarily, linear and follows the form

$$\tau_{\text{index}} = a_1 \tau_{\text{instrument}} + a_0. \quad (3)$$

The slope a_1 is determined by calculating both $\tau_{\text{instrument}}$ and τ_{index} from historical hydrographic profiles. The offset a_0 is obtained from a hydrographic profile sampled during the PIES deployment, and is defined as the difference between the τ_{index} measured through the hydrocast (later called τ_{CTD}) and $a_1 \tau_{\text{instrument}}$ obtained concurrently by PIES. In the case when several hydrographic profiles are available during the PIES's deployment, an offset that minimizes the difference between τ_{CTD} and τ_{index} is calculated, and the sum of squared residuals is defined as

$$\epsilon = \sum \{\tau_{\text{CTD}}(i) - [a_1 \tau_{\text{instrument}}(i) + a_0(i)]\}^2. \quad (4)$$

The error associated with the steps described in Eqs. (3) and (4) stems from the mismatch in the location and timing of the PIES measurement and the hydrographic cast, and measurement errors. Measurement errors comprise both the errors in the temperature, conductivity, pressure observations from the CTD, and in pressure and τ recorded by the PIES.

In addition to these error sources is an error associated with the unaccounted τ variability between the reference depth of τ_{index} and the instrument depth. This error may be large for cases where an instrument is located far deeper than the reference depth, such as H4. The bias error in τ_{index} at the instrument sites propagates as an error in the gridded results through the mapping of the mean field. A higher number of deep hydrographic casts (to determine a_1) and of casts reaching at least to the reference depth during the deployment (to determine a_0) can increase the accuracy, but one of the challenges presented by the study region northeast of Luzon is the limited number of hydrographic profiles that reach to the depths of the deepest instruments. This makes the conventional τ conversion process at station H4, which exceeds 4000-m depth, particularly susceptible to error.

In addition to the errors associated with conversion to τ_{index}, the mapping itself may also constitute a significant source of error. In the objective mapping process, the time mean of each PIES record is first removed prior to mapping the daily residual field. A $\tau_{\text{mean PIES}}$ field is determined by linearly interpolating the time-averaged τ_{index} of each PIES site onto a 10-km grid [in our case we use the Barnes interpolation (Barnes 1964) to include the northernmost station, H5, in the interpolation calculations], and this is subsequently added to the objectively mapped residual field to produce the final daily maps of τ_{index}. If the instrument spacing is large relative to the distance over which the time-mean pycnocline slope varies, then smoothing between instrument pairs will prevent accurate calculation of the baroclinic velocities in sharp frontal areas such as those typical of western boundary currents. This is the case along the Kuroshio, as the front separating South China Sea waters from North Pacific waters spans around a $O(10^1)$ km width (Mensah et al. 2014; Jan et al. 2015), which is roughly 2–3 times shorter than the typical spacing of PIES instruments.

Finally, in addition to the errors in converting from τ to τ_{index} and the mapping errors, the GEM lookup tables (Fig. 2a) include some uncertainty as illustrated in Fig. 2b, which displays the root-mean-square (rms) error of the temperature GEM as a function of depth and τ_{index}. The rms error is defined as the difference, in each τ_{index} and depth bin, between the GEM-inferred temperature and the temperature actually measured by a CTD cast or Seaglider dive. The largest discrepancies are found in the range of 1.0575–1.0600 s within the upper 200 m, and reach 2°C. Relatively large errors up to 1°C persist within the upper 300 m for lower τ values. Below these depths, the errors are mostly uniform and generally do not exceed 0.5°C.

Some of the errors in the GEM lookup tables for the region near Luzon are likely due to the different
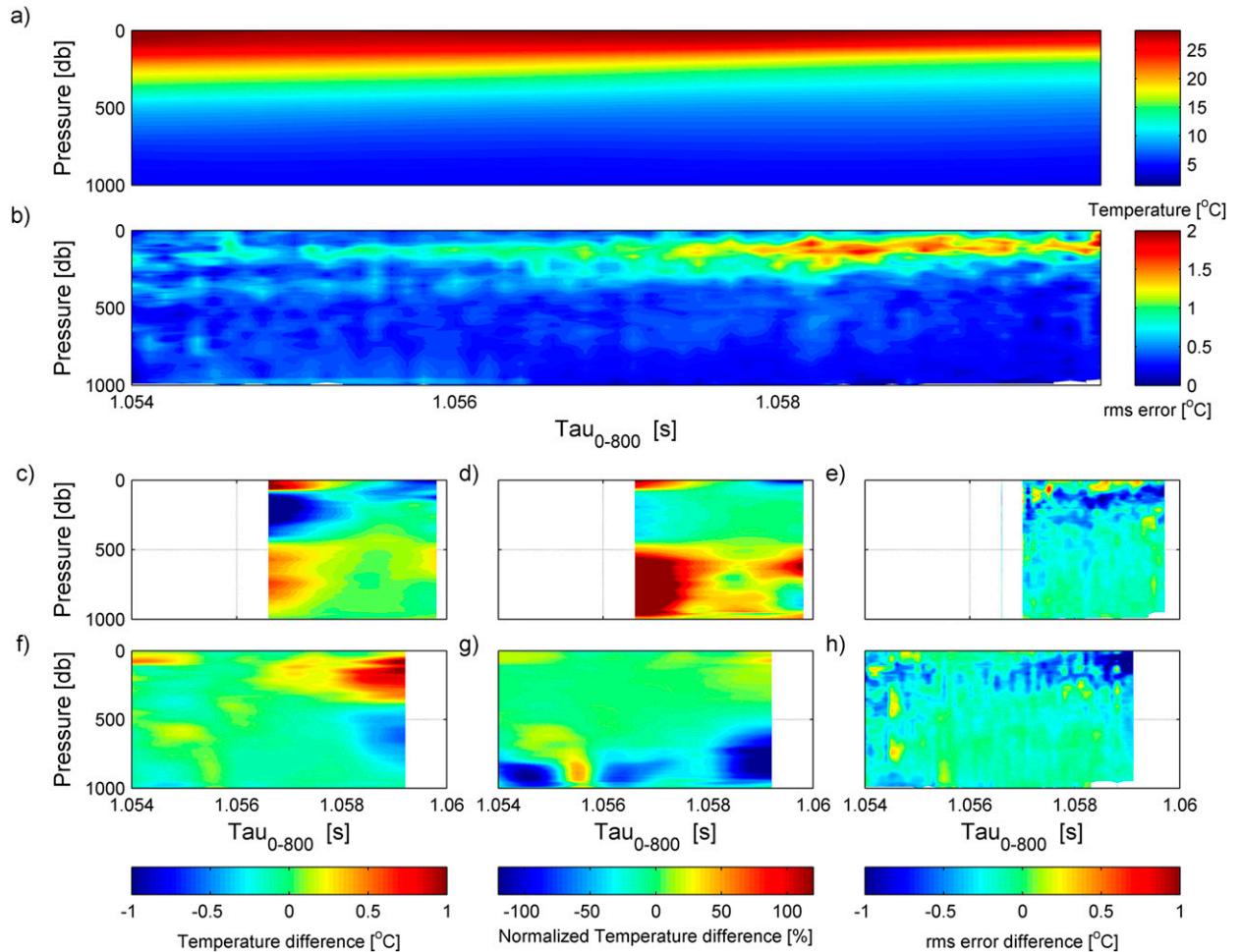
FIG. 2. (a) Full-domain temperature GEM and (b) its rms error; (c) temperature difference, (d) normalized temperature difference, and (e) rms error difference between the western GEM and the full-domain GEM. (f)–(h) As in (c)–(e), but for the difference between the eastern GEM and the full-domain GEM. In subsequent estimates, the GEM in (a) is used for the $\tau_{\text{mean SG}}$ case, whereas the western and eastern GEMs are used in the $\tau_{\text{mean SG\_EW}}$ estimates.

water masses present within the region. Indeed, the area northeast of Luzon communicates with the South China Sea via the Babuyan Channel. Waters of South China Sea (North Pacific) origin are observed west (east) of 122.3°E (Lien et al. 2015, their Fig. 5). Between ~100 and ~300 m, South China Sea Tropical Water (SCSTW) is colder and fresher than the North Pacific Tropical Water (NPTW) transported by the Kuroshio (Mensah et al. 2014). Conversely, between 400 and 800 m, South China Sea Intermediate Water (SCSIW) is saltier than the North Pacific Intermediate Water (NPIW) (Chen and Wang 1998; Chen 2005; Mensah et al. 2015) and slightly warmer below 600 m (Figs. 3a and 3b). These different water masses yield similar τ_{index} values for quite distinct hydrographic profiles, resulting in the higher error described above.

c. Modifications to the standard process

1) MAPPING τ_{INDEX} BASED ON REGIONAL HYDROGRAPHY

To mitigate the errors outlined above that arise from the standard τ conversion and mapping processes, we adopt two modifications to the processing routine: 1) we modify the mapping and 2) we generate two separate GEMs for the areas influenced by different water masses. First, in the mapping step, a mean τ_{index} field derived from historical hydrographic profiles is substituted for the mean τ_{index} field obtained by simply interpolating between the PIES [section 2b(1)]. This modification therefore bypasses the errors associated with the τ conversion [Eq. (3)]. In addition, the spatial resolution of the mean field will be improved, as the
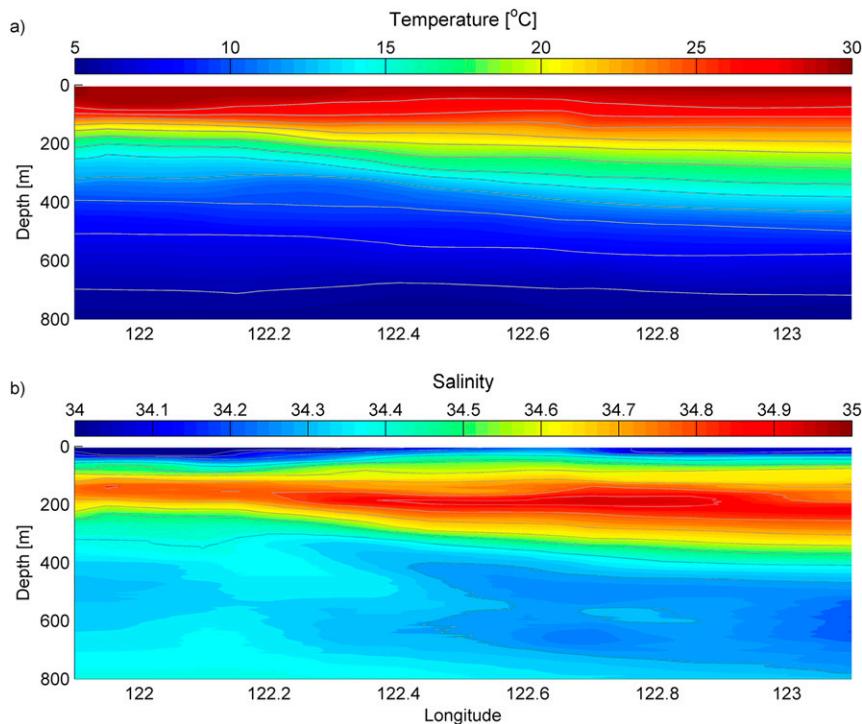
FIG. 3. (a) Averaged temperature and (b) salinity measured by the Seaglider along 18.75°N between November 2012 and May 2013.

τ_{index} value in each grid cell is calculated from actual data instead of being the result of a linear interpolation between PIES instruments separated by ~30 km. We therefore expect that the density gradients across the PIES array will be better represented.

Two different hydrography-based mean fields are tested for the region northeast of Luzon. A mean field based on all hydrographic data (Seaglider, Argo, and ship-based casts), $\tau_{mean\,SG}$, is calculated from the τ_{index} of all the hydrographic casts used to establish the GEM. Since this dense hydrographic dataset northeast of Luzon is dominated by the influence of Seaglider data taken during the PIES experiment (which may not be available for other PIES field programs), we also calculate a mean τ field using only an "historical" dataset ($\tau_{mean\,Hist}$), which includes the 117 historical casts, supplemented by 39 randomly picked Seaglider profiles. In this historical dataset, just enough Seaglider profiles are included to increase the data density such that there are about eight profiles within a 15-km diameter of each grid point. These fields are compared to the $\tau_{mean\,PIES}$, that is, the PIES-based mean τ_{index} (section 2b).

For both of these hydrography-based mean fields, $\tau_{mean\,SG}$ and $\tau_{mean\,Hist}$, the optimum zonal xr and meridional yr smoothing length scales for the Barnes interpolation are chosen according to the method described in the appendix. The hydrography-based mean fields ($\tau_{mean\,SG}$ or $\tau_{mean\,Hist}$) and $\tau_{mean\,PIES}$ fields have marked differences. In particular, the τ value at H4 differs by 0.7 ms between the $\tau_{mean\,PIES}$ and $\tau_{mean\,SG}$ fields (Figs. 4a and 4c), which is likely due to a large error in determining the PIES τ_{index} at this location, where few full-depth hydrographic profiles are available for the standard τ conversion process [i.e., a_1 in Eq. (3) is not well constrained].

2) SEPARATE GEMs ACROSS THE WATER MASS FRONT

The second adaptation in the processing method is the use of separate GEMs for the eastern and western regions of the array to reduce the GEM-induced error in converting τ_{index} to hydrographic profiles northeast of Luzon. Two GEMs are generated from the combined Seaglider and historical cast datasets: one is an eastern GEM with data selected between 122.3° and 123.5°E, which includes 1231 profiles; and the other is a western GEM comprising 476 profiles located between 121.75° and 122.3°E.

These two GEMs are noticeably different from the single GEM as illustrated by Fig. 2c–h. The temperature difference between the western GEM and the full-domain
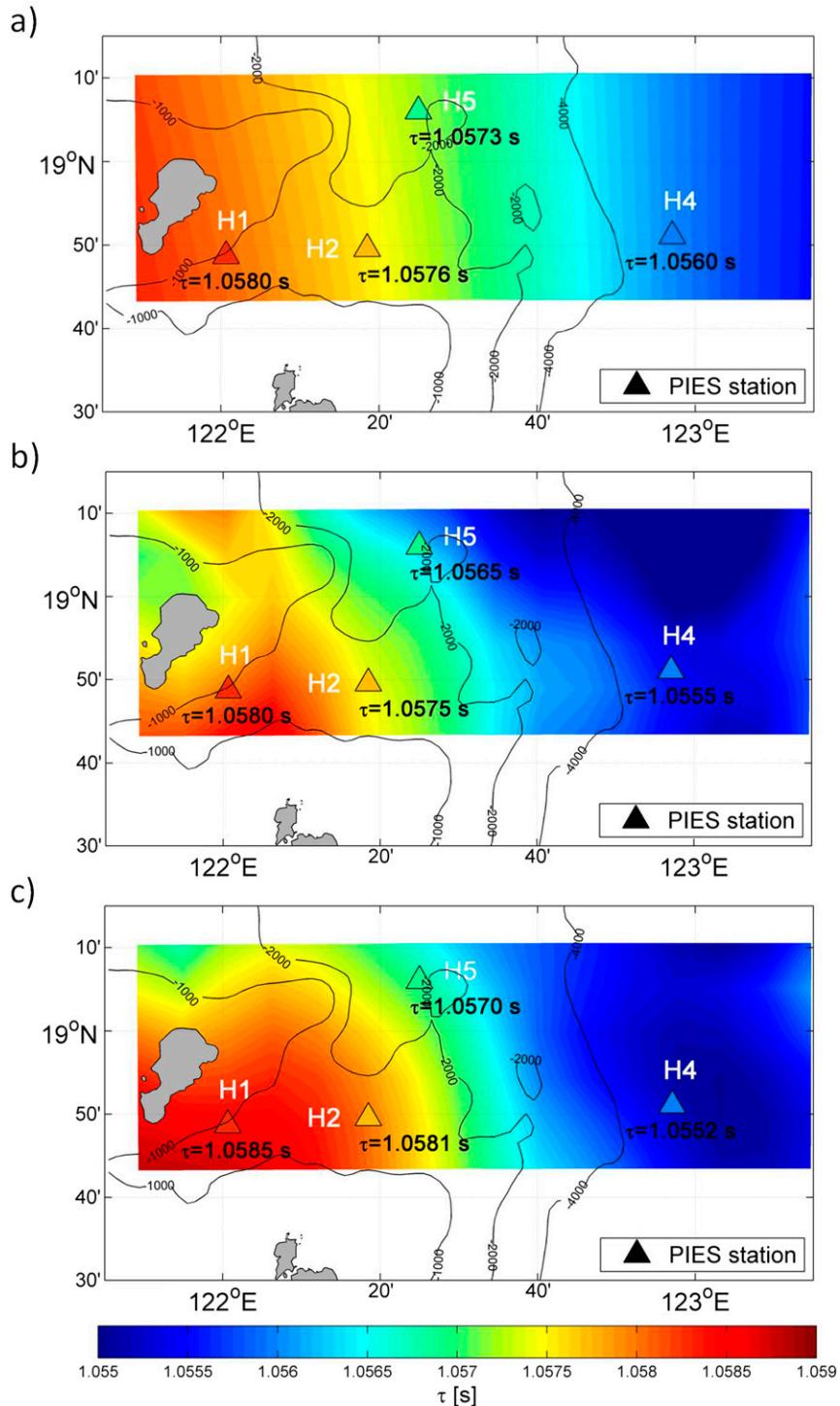
FIG. 4. Mean τ field calculated from (a) PIES time series, (b) historical hydrographic data, and (c) Seaglider complemented with historical data.

GEM (Fig. 2c) exhibits sharp contrasts for the range $1.0565\,\text{s} \le \tau_{\text{index}} \le 1.0580\,\text{s}$, with large negative values at depths of tropical waters, and positive values at the intermediate (and surface) water depths. These

differences imply that the western GEM includes mostly the South China Seawater profiles with their colder tropical waters and warmer intermediate waters, as suggested in Fig. 5 of Lien et al. (2015). Conversely,

subtracting the full-domain GEM from the eastern GEM (Fig. 2f) yields broad variations in the range $1.057 \, \mathrm{s} \leq \tau_{\mathrm{index}} \leq 1.059 \, \mathrm{s}$. The positive (negative) difference at the depths of the tropical (intermediate) water demonstrates that the eastern GEM includes mostly waters of North Pacific origin. Moreover, the normalized temperature differences (Figs. 2d and 2g)—calculated at each depth as the temperature difference divided by the temperature range at this level—are high below 500 m. Similarly, because horizontal differences in specific volume anomaly are also found (not shown), the current shear at large depths inferred from τ_{index} should be greatly impacted by the splitting of the GEMs into eastern and western subregions.

As a result of these property distributions, the lookup tables' uncertainty is impacted, with the GEM rms error considerably lower for both the eastern and western GEMs (as compared to the single GEM) between 100 and 300 m, that is, the largest error band (Figs. 2e and 2h). For the western GEM, larger errors appear in patches in the upper 80 m, yet over the whole τ domain and between the surface and 800-m depth, the error decreases (relative to the single GEM) on average by 38% for the western GEM and 37% for the eastern GEM. This marked improvement supports the use of separate GEMs in this frontal region. Similar patterns and corrections are also obtained for the specific volume anomaly GEMs (not shown). The two-GEM solution is implemented northeast of Luzon by converting the mapped daily τ_{index} west of 122.2°E to temperature profiles (and specific volume anomaly profiles) with the western GEM, and east of 122.4°E with the eastern GEM. The profiles of the remaining grid cell at 122.3°E are obtained by linear interpolation of the profiles west and east of this cell.

Note that another multiple-GEM technique has been devised by Park et al. (2005). In that case, the multi-index GEM procedure addressed the issue of important temporal variability in the mixed layer depth of the southwestern Sea of Japan/East Sea. Here two sets of GEM tables were used alternatively based on climatological information. This led to a strong decrease in the error associated with the GEM temperature and specific volume anomaly fields. In our study region, the spatial rather than temporal variability dominates, supporting our use of geographically separated GEMs.

d. Absolute velocities and transports obtained by leveling PIESs with ADCPs

Horizontal gradients in specific volume anomaly profiles, whether inferred from PIESs and the GEMs or whether measured directly (e.g., by a Seaglider, Argo float, or shipboard cast), can be used to calculate the

geostrophic velocity shear V_{BC} between hydrographic profiles relative to a reverence level (e.g., 800 dbar) using Eq. (2). To make these velocity shears absolute, however, a reference geostrophic velocity at some level must be known; an absolute velocity can be inferred from the horizontal pressure gradient along a suitable geopotential surface. Since PIESs generally cannot be deployed onto a common geopotential surface (e.g., northeast of Luzon, the depth of neighboring PIESs differed by up to 2500 m), it is first necessary to level the PIESs' pressure sensors. Through leveling, neighboring pressure records are projected onto a common geopotential surface.

In previous applications, deep current sensors near the PIESs provided the reference velocity used to level the PIESs (e.g., Watts et al. 2001). In the experiment northeast of Luzon, the ADCP array, with its upward-looking ADCPs at 450-m depth, provides suitable velocities for the PIES leveling procedure. The time means of the ADCP-measured velocities at 400-m depth are chosen, since this is sufficiently deep to avoid a time-mean ageostrophic velocity associated with a surface Ekman layer. Results of a sensitivity test (not shown) suggest that the leveling and the resulting absolute velocity estimates are insensitive to the choice of ADCP velocities from depths between 350 and 450 m. The procedure is demonstrated in Fig. 5 specifically for the velocities between instruments H1 and H2, but it is representative of the procedure applied across the Kuroshio.

The region's GEMs use a reference level of 800 dbar, so H1 and H2 must be leveled to find $V_{\mathrm{Abs}}(t, 800)$, the time-varying absolute geostrophic velocity at $z = 800 \, \mathrm{m}$. Here z is a geopotential (level) surface, and it is assumed that there is negligible shear between the 800-dbar pressure surface and the 800-m geopotential surface. In practice, the geopotential levels at which the PIES instruments are deployed (i.e., $z = -d_1$ and $z = -d_2$ for H1 and H2, respectively) cannot be known exactly. But they are each time invariant, since the PIESs are fixed relative to the seabed.

Assuming geostrophy and considering the time mean over a period T,

$$\overline{V}_{\mathrm{Abs}}(800) = \frac{1}{\rho f l} \frac{1}{T} \sum_{t=0}^{T} \left[p_2(t) - p_1(t) \right] - \frac{\rho_o g D}{\rho f l} - \varepsilon \\ - \frac{1}{T} \sum_{t=0}^{T} \int_{-d_i}^{-800\mathrm{m}} \left[V_{\mathrm{BC}}(t, z) \right] dz. \qquad (5)$$

Here p_2 and p_1 are the pressures measured by the PIESs at H1 and H2, which are separated by a horizontal distance l. The vertical distance D is between H2 and H1
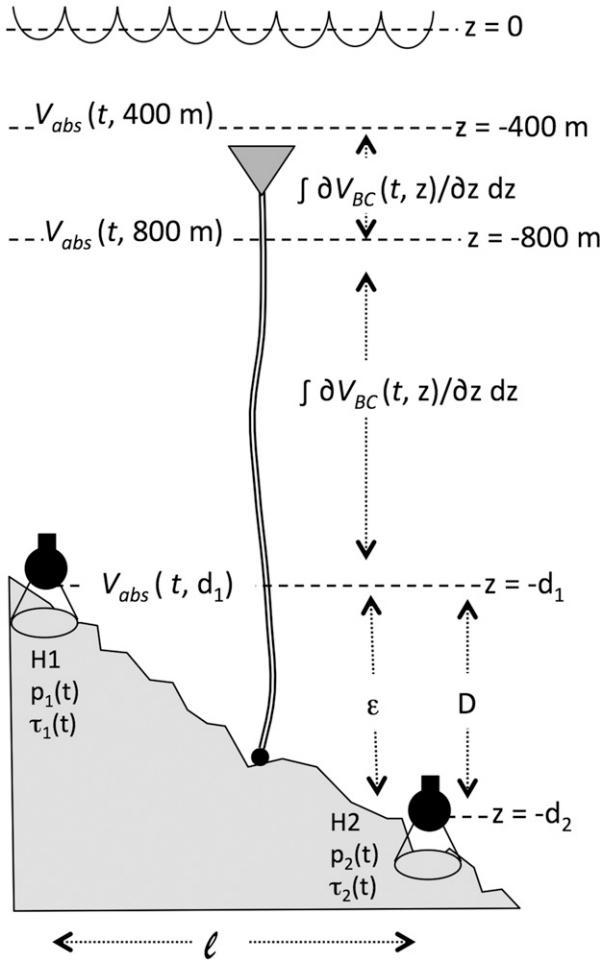
FIG. 5. Schematic of the leveling procedure leading to the determination of absolute velocity current between PIES instruments H1 and H2. The procedure involves the use of PIES pressure and baroclinic current shear, and a reference velocity provided by an ADCP.

(i.e., $D = d_2 - d_1$), and ε is a small correction term related to the very deep shear. Together, the first three terms on the RHS give the time-mean absolute velocity at $z = d_1$ at a location between H1 and H2, $\overline{V}_{\text{Abs}}(d_1)$. The final term on the RHS is the time-mean shear between 800 m and $z = d_1$; this term can be determined from τ measured at H1 and H2, the GEMs, and Eq. (2).

The error term in Eq. (5) ε accounts for the shear between d_1 and d_2 at H2. Though there is weak stratification in the deep ocean, the deep shear here can be nonnegligible, particularly if D is large. It is given by

$$\varepsilon = \frac{1}{T} \sum_{t=0}^{T} \int_{-d_2}^{-d_1} \frac{\partial [V_{\text{BC}}(t,z)]}{\partial z} dz. \tag{6}$$

Although the mean of the deep shear is nonnegligible, its variation in time is neglected here (since D is constant).

The term $\overline{V}_{\text{Abs}}(800)$ is also related to the ADCP-measured velocity at 400 m and the shallow shear. Again, considering the time mean (and assuming that the ageostrophic contributions to the ADCP-measured velocity are canceled by the averaging),

$$\overline{V}_{\text{Abs}}(800) = \frac{1}{T} \sum_{t=0}^{T} V(t,400)$$
$$+ \frac{1}{T} \sum_{t=0}^{T} \int_{-800\text{m}}^{-400\text{m}} \frac{\partial [V_{\text{BC}}(t,z)]}{\partial z} dz. \tag{7}$$

Here, the first term on the RHS is from the time-mean ADCP record and the second term is the time-mean shear between 400 and 800 m determined from τ measured at H1 and H2 and the GEMs.

Combining Eqs. (5) and (7) leaves only two terms that cannot be determined by the PIESs' and ADCP's time-mean records. These two terms are combined into a time-invariant leveling constant relating H1 and H2, LC. For convenience the term is cast so it also includes the time means of the PIESs' pressure records, $\overline{p}_1$ and $\overline{p}_2$:

$$\text{LC} = \overline{p}_2 - \overline{p}_1 - \rho_0 g D - \varepsilon \rho f L \tag{8}$$

In fact, the ε term is of $O(10^{-3} - 10^{-2})\,\text{m s}^{-1}$ and may not be accurately determined because of uncertainty in the GEM. LC is calculated iteratively instead. The initial term LC_t is obtained through the combination of Eqs. (5) and (7) omitting ε:

$$\text{LC}_t = \left\{ \frac{1}{T} \sum_{t=0}^{T} V(t,400) + \frac{1}{T} \sum_{t=0}^{T} \int_{-di}^{-400\text{m}} \frac{\partial [V_{\text{BC}}(t,z)]}{\partial z} dz \right\} \rho f L; \tag{9}$$

ε is subsequently determined as the difference between this first estimate of leveled PIES velocity and the ADCP velocity:

$$\varepsilon = \left(\frac{\text{LC}_t}{\rho f L} - \frac{1}{T} \sum_{t=0}^{T} \int_{-di}^{-400\text{m}} \frac{\partial [V_{\text{BC}}(t,z)]}{\partial z} dz \right)$$
$$- \frac{1}{T} \sum_{t=0}^{T} V(t,400). \tag{10}$$

Equation (8) is subsequently solved. With this LC determined from the time-mean τ and ADCP records, the time-varying reference velocity between H1 and H2 can now be calculated from PIESs' pressure and τ observations (without relying on the time-varying ADCP record, which might include ageostrophic contributions in the instantaneous measurements):

TABLE 1. Thermocline depth rms error for four procedures of the PIES processing as described in section 3.

	Mean field	Longitude										
		122°	122.1°	122.2°	122.3°	122.4°	122.5°	122.6°	122.7°	122.8°	122.9°	123°
Thermocline depth	$\tau_{\text{mean PIES}}$	44.0	42.4	37.9	32.2	20.2	18.3	16.7	16.3	16.7	18.0	19.9
rms error (m)	$\tau_{\text{mean Hist}}$	44.0	30.1	30.6	32.8	24.1	18.2	16.5	15.2	9.0	8.5	11.1
	$\tau_{\text{mean SG}}$	26.2	25.3	23.2	21.0	18.5	19.6	14.9	9.3	10.3	9.6	11.1
	$\tau_{\text{mean SG\_EW}}$ (2 GEMS)	23.2	19.5	16.3	19.9	19.3	16.3	12.8	9.3	9.3	8.7	11.7

$$\overline{V}_{\text{Abs}}(800) = \frac{1}{\rho f L}[(p_2'(t) - p_1'(t)) + \text{LC}]$$
$$- \int_{-di}^{-800\text{m}} \frac{\partial[V_{\text{BC}}(t,z)]}{\partial z} dz \qquad (11)$$

While ε accounts for the time-averaged inaccuracies resulting from the unaccounted shear between D1 and D2, it does not correct the time-varying errors such as those arising from the drift of the PIES pressure sensor. We recommend that prior to applying the leveling procedure, pressure drift should be corrected according to the method described in Kennelly et al. (2007).

3. Evaluating the processing schemes

To evaluate the amended mapping and GEM lookup table procedures, the PIES-derived hydrographic structure and current shear inferred from τ_{index} are compared with properties and currents directly measured by the Seagliders and ADCPs, respectively. The four tested procedures are 1) the original processing method in which the τ mean field is derived from PIES measurements, $\tau_{\text{mean PIES}}$; 2) an amended method using a single GEM and a mean field derived from the historical dataset, $\tau_{\text{mean Hist}}$; 3) as in procedure 2, but with the mean field derived from all the available hydrography (which is primarily Seaglider data acquired during the experiment, supplemented with historical CTD data), $\tau_{\text{mean SG}}$; and 4) a two-GEM solution, using the mean field as in procedure 3 (Seaglider), $\tau_{\text{mean SG\_EW}}$. Below, the thermocline depths inferred from the PIES measurements via these four procedures are compared with the thermocline depths observed by the Seaglider. Further, the vertical shears calculated from the specific volume anomaly profiles obtained via the four PIES processing procedures are also compared with the Seaglider-derived shear profiles. Finally, the baroclinic (relative) geostrophic volume transports are calculated and compared for both PIES and Seaglider sections.

a. Thermocline depth and current shear

The different processing methodologies are first evaluated with respect to their ability to accurately reproduce the depth of the thermocline across the Kuroshio as compared with Seaglider observations. Between 29 November 2012 and 31 May 2013, 15 Seaglider sections were acquired across the Kuroshio, and based on these observations, we define the thermocline depth as the depth of the 16°C isotherm, which is the most steeply sloped isotherm across the sections. For all 15 sections, and at each grid cell, the average depth difference between the thermocline measured by the Seaglider and that inferred from the mapped τ_{index} (and the temperature GEM) is calculated (Table 1). The rms error averaged over the 11 grid cells separating H1 and H4 yields 25.7 m for $\tau_{\text{mean PIES}}$, 21.8 m for $\tau_{\text{mean Hist}}$, and 17.2 m for $\tau_{\text{mean SG}}$, which represents a decrease in error of 15% and 33%, respectively. The maximum decrease is obtained with $\tau_{\text{mean SG\_EW}}$, with an rms error of 15.1 m, or an error drop (relative to the standard processing procedure) of 41%.

The improved thermocline estimates are illustrated in Fig. 6, which displays the isotherm contours obtained from a representative Seaglider section in each panel (shading and black contours) and the isotherms derived from the contemporaneous PIES observations using the four different τ processing procedures (white contours in Figs. 6a–d). The amended mapping and GEM procedures (Figs. 6b–d) improve not only the structure of the thermocline (16°C isotherm) relative to the standard procedure (Fig. 6a), but also the temperature structure at other depths. The rendering of the whole hydrographic structure is improved when using the hydrography-based mean fields, and the best results are obtained with $\tau_{\text{mean SG}}$ and $\tau_{\text{mean SG\_EW}}$. While the use of $\tau_{\text{mean SG\_EW}}$ episodically deteriorates the depth determination of the uppermost isotherms compared to $\tau_{\text{mean SG}}$, it systematically improves that of all the other isotherms, especially those below 500 dbar (e.g., Figs. 6c and 6d). These improvements through the amended processing schemes are also valid when considering results in terms of specific volume anomaly profiles (not shown).

As expected, the improved thermocline depth estimates are accompanied by a better determination of the horizontal density gradients across the array, and hence of the vertical shear in the horizontal currents. To
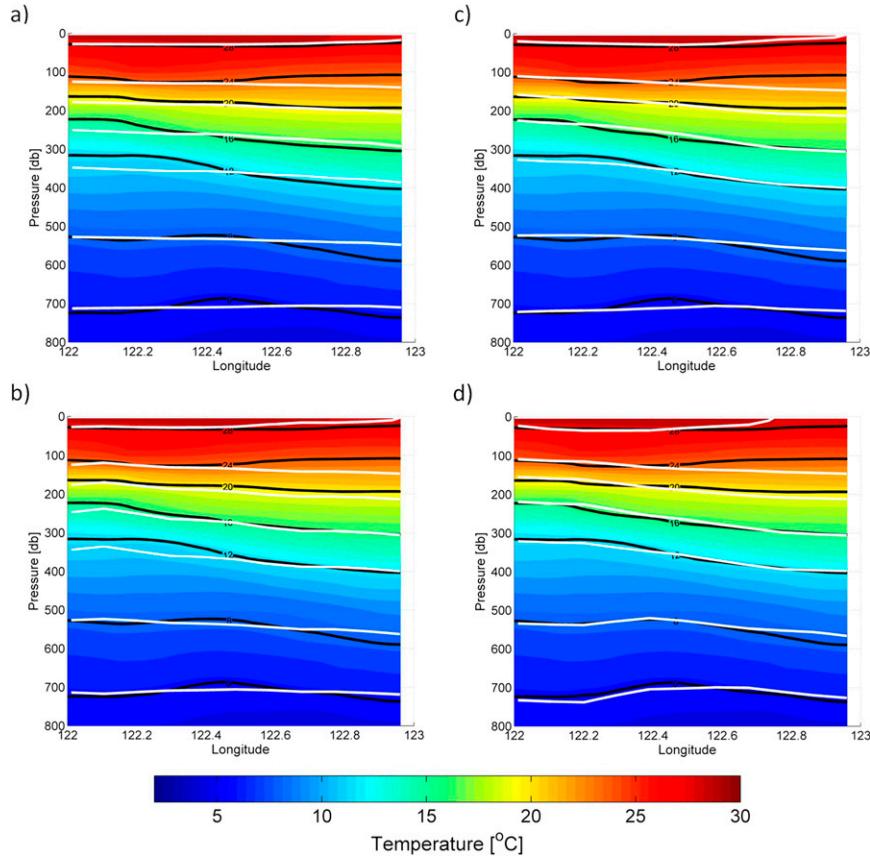
FIG. 6. Temperature section measured by Seaglider between 22 and 27 Apr 2013. The black contours represent the isotherms measured by the Seaglider, and the white contours are those same isotherms derived from the PIES array processed with four different procedures: τ mean field from (a) PIES ($\tau_{\text{mean PIES}}$), (b) historical hydrographic data ($\tau_{\text{mean Hist}}$), (c) seaglider ($\tau_{\text{mean SG}}$), and (d) seaglider and two separate GEMs for converting τ to temperature profiles ($\tau_{\text{mean SG\_EW}}$).

quantify the improvement with respect to the velocity shear achieved through the amended procedures, we calculate the velocity shear derived from Seaglider measurements during each of its 15 cross sections [using measured temperature and salinity profiles, and thermal wind relation, Eq. (2)]. Subsequently, we compare this shear with that obtained simultaneously from $\tau_{\text{mean PIES}}$ and $\tau_{\text{mean SG\_EW}}$ (and $\tau_{\text{mean SG}}$). The results calculated between the surface and 800 m (Table 2) show that the error decreases in each grid cell between 122.1° and 122.9°E. The error is reduced by 22% across the whole array and by nearly 40% near the center of the section, where the shear is the largest.

b. Baroclinic volume transport

We compare the baroclinic (relative) volume transport obtained from the four different processing methodologies with that obtained from the Seaglider during each of its 15 cross sections (Fig. 7). The baroclinic

volume transports are calculated by integrating velocity shears from 0 to 1000 dbar and from 122.10° to 122.87°E, and are calculated relative to an 800-dbar-level of no motion. To account for the temporal mismatch between the ~6–12-daylong Seaglider sections and the twice-daily PIES estimates, the 15 corresponding PIES-derived transports are averaged within ±2 days of the median date of each Seaglider crossing.

The baroclinic transports obtained from $\tau_{\text{mean PIES}}$ are generally lower than the Seaglider transports, exhibiting an rms difference of 7.8 Sv ($1 \, \text{Sv} \equiv 10^6 \, \text{m}^3 \, \text{s}^{-1}$). The PIES results processed with the Seaglider-based mean fields are closer to the Seaglider-derived transports, with an rms difference of 3.6 Sv ($\tau_{\text{mean SG}}$) and 3.4 Sv ($\tau_{\text{mean SG\_EW}}$). The $\tau_{\text{mean Hist}}$-processed data yield an intermediate error of 5.5 Sv. While the difference between the PIES-derived and Seaglider-derived baroclinic transports is considerably reduced with the use of $\tau_{\text{mean SG}}$, it remains significant, as it represents around 20% of the average

TABLE 2. Baroclinic shear (from surface to 800 dbar) and rms error of shear at each grid cell, as obtained from the original procedure ($\tau_{\text{mean PIES}}$), a seaglider based τ mean field ($\tau_{\text{mean SG}}$) and the seaglider based mean field associated to two separate GEMs for converting τ to specific volume anomaly profiles ($\tau_{\text{mean SG\_EW}}$).

| | | Longitude | | | | | | | | |
		122.1°	122.2°	122.3°	122.4°	122.5°	122.6°	122.7°	122.8°	122.9°
	Shear ($10^{-3}\,\text{s}^{-1}$)	0.8	1.0	1.1	1.1	1.1	0.9	0.7	0.5	0.3
Normalized error	$\tau_{\text{mean PIES}}$	0.78	0.72	0.69	0.68	0.68	0.76	0.72	0.63	0.66
	$\tau_{\text{mean SG}}$	0.72	0.60	0.53	0.48	0.45	0.55	0.60	0.59	0.64
	$\tau_{\text{mean SG\_EW}}$	0.69	0.56	0.48	0.43	0.43	0.53	0.60	0.58	0.61

baroclinic transport. This difference could be explained, in part, by the aliasing generated by the Seaglider, as it usually takes 6–12 days to complete a cross section, as well as the residual error in the GEM. In spite of the ~3.5-Sv rms difference between the PIESs' and Seaglider's baroclinic transports during the 15 discrete sections, the baroclinic transports averaged over the time of the 15 Seaglider sections are very close to the PIES-derived transport averaged over the same timing, with 15.6 Sv estimated by the Seaglider, 14.5 Sv with $\tau_{\text{mean SG}}$, and 14.7 Sv with $\tau_{\text{mean SG\_EW}}$.

c. Absolute volume transport

The PIES-derived absolute volume transports [calculated from $\overline{V}_{\text{Abs}}(800)$, the reference absolute velocity at 800 m in (11)] are evaluated here through two independent comparisons. First, 15 PIES-derived estimates are compared with absolute transports obtained from the contemporaneous 15 Seaglider sections (Fig. 8a). For this comparison the Seaglider-derived shears are referenced using the glider's vertically averaged currents (e.g., Todd et al. 2011) and the absolute volume transports are all calculated for the layer from

the surface to 1000 dbar (which is the vertical limit of the glider dives). The second comparison is made between the absolute transport time series derived from the PIES and that determined from the ADCP moorings along the M line (Fig. 8b). In this case, transports are for the layer between the surface and 600 dbar, following Lien et al. (2014), who extrapolate their ADCP measurements to these levels in order to capture a larger part of the Kuroshio transport. In both comparisons, the zonal integration range is set to 122.10°–122.87°E, which corresponds to the zonal extent of the ADCP array.

The 0–1000-dbar-layer transport time series derived from the PIESs (Fig. 8a) show that, regardless of the mean τ_{index} field used, all absolute transports obtained from a single GEM compare less well with the Seaglider-derived transport than do those calculated from a two-GEM solution. The best agreement between the PIESs' and the Seaglider's absolute transport estimates is indeed obtained with $\tau_{\text{mean SG EW}}$ yielding an rms difference of 1.8 Sv between PIES-derived and Seaglider-derived values. The occasional large differences between the $\tau_{\text{mean SG}}$ and $\tau_{\text{mean SG EW}}$ transport estimates (relative to the Seaglider-derived estimates)
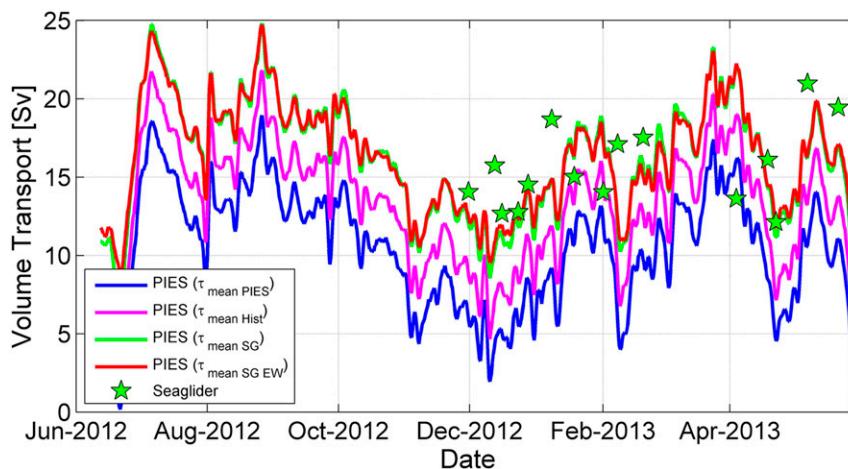

FIG. 7. Time series of the Kuroshio baroclinic volume transport obtained from the PIES four different processing procedures and the 15 Seaglider sections. The volume transport was integrated between 122.10° and 122.87°E and from surface to 1000 m, relative to 800 m.
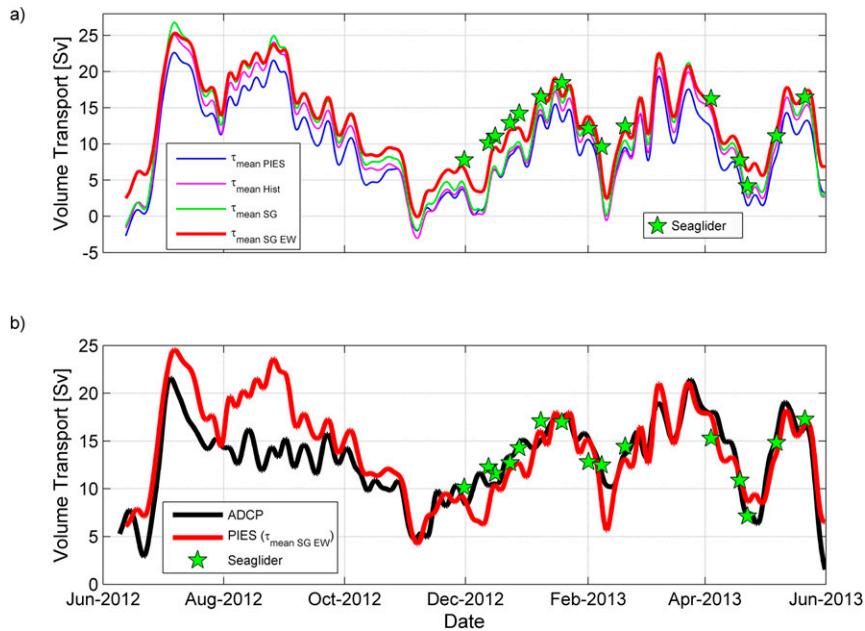
FIG. 8. (a) Time series of the Kuroshio absolute geostrophic volume transport obtained from the four different PIES processing procedures and the 15 Seaglider sections, with all transports integrated between 0 and 1000 dbar. (b) Integrated 0–600-dbar volume transport time series derived from the six ADCP moorings of the M line (black), from the PIES processed with $\tau_{\mathrm{mean\,SG\,EW}}$ (red), and from the Seagliders (green stars). All volume transports in (a) and (b) were integrated between 122.10° and 122.87°E. In (a), note that some of the curves overlay some periods of time.

demonstrates that the choice of a single GEM or separate GEMs is crucial in impacting the absolute velocities estimates. This is surprising in light of the limited influence of two GEMs on the integrated baroclinic velocity results (section 3b).

The comparison between the 0–600-dbar absolute transport time series derived from the ADCPs and that from the PIESs with $\tau_{\mathrm{mean\,SG\,EW}}$ (Fig. 8b) yields an rms difference of 3.0 Sv. The average transport is 13.1 Sv for the ADCP-derived transports (i.e., the total transport with geostrophic and ageostrophic contributions) and 14.2 Sv for the (leveled) PIES-derived transports (i.e., the absolute geostrophic transport). The mismatch between the two time series is particularly large from July to the middle of September 2012. Thereafter, the PIES and ADCP transports agree well with only short periods of mismatch.

4. Discussion

a. Sensitivity of the transport estimates to the mean τ_{index} field

The comparisons of PIES, Seaglider, and ADCP datasets demonstrate that the amended procedures for mapping the τ_{index} led to substantial improvement in

determining the hydrographic structure and baroclinic volume transports from PIESs. The use of separate GEMs further improves the thermocline depth determination at some locations northeast of Luzon. The baroclinic volume transport comparison delineated in section 3b, however, exhibits no marked difference between the time series obtained with a single GEM or separate GEMs. This implies that the use of separate GEMs has little influence on the depth- and distance-integrated result, and that the choice of the mean τ_{index} field is the crucial element in determining the accuracy of volume transport estimates between two fixed endpoints. This can be explained by the amplitude of the zonal gradient of τ_{index} determined by the different mapping methodologies. The difference of τ_{index} between H1 and H4 is only 2 ms when using $\tau_{\mathrm{mean\,PIES}}$, (Fig. 4a), but it reaches 3.2 ms with $\tau_{\mathrm{mean\,SG}}$ (Fig. 4c). This difference led to the 7.8- and 3.4-Sv rms difference with the Seaglider-derived transport (Fig. 7). It appears that the much narrower τ_{index} range obtained from the original processing method is due to the underestimation of τ_{index} at the westernmost station and its overestimation at the easternmost location. Since processing the data with $\tau_{\mathrm{mean\,SG\,EW}}$ uses the same τ field as $\tau_{\mathrm{mean\,SG}}$, no significant volume transport difference
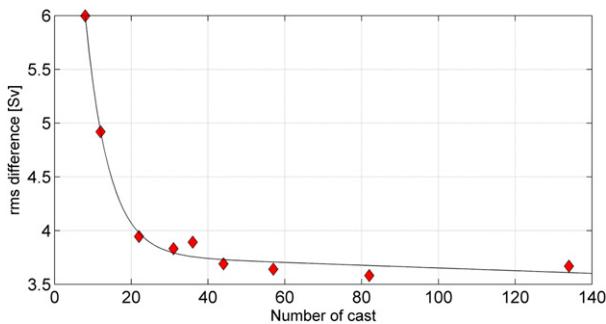
FIG. 9. Average number of casts available for the objective mapping of each grid cell along the PIES array vs rms difference of baroclinic volume transport, referred to as the 15 Seaglider transport estimates. A two-term exponential model is fitted to the data (solid black curve).

exists between the two methods. For the historical data–based field, the west–east τ_{index} difference amounts to 2.8 ms. As a result, $\tau_{mean\,Hist}$ yields significantly better results than the PIES-derived mean field, but it still presents a volume transport rms difference of 5.4 Sv (Fig. 7). The relatively high error might be due to the poor sampling density of this historical data field, which contains only 157 profiles in an area of $\sim$10 000 km^2. To clarify this issue, we calculate the PIES-derived baroclinic volume transports obtained from nine different τ mean fields, each of these including a different number of Seaglider casts. The rms difference with the Seaglider transports is subsequently estimated. To facilitate the comparison, all τ mean fields are calculated with similar smoothing values for the Barnes interpolation, $xr = 0.15°$, $yr = 0.15°$ (see the appendix). For each of the 10 grid cells separating H1 from H4, we determine the number of casts included within a $xr/2$ radius centered on each of the grid cells and calculate an average of these 10 values. This average number of casts available for the Barnes interpolation is then plotted against the volume transport rms difference as shown in Fig. 9. Based on these results, it appears that the rms difference exponentially drops, with a 2 e-folding scale of 23 profiles.

The high errors initially generated by the use of $\tau_{mean\,PIES}$ are also mainly caused by the very poor sampling in the region northeast of Luzon and the limited number of data for conducting the τ conversion operations. In particular, H4, a crucial instrument, as it is the easternmost station of the array, is located at more than 4000-m depth, where only 32 deep stations were available for the determination of the slope a_1 [Eq. (3)]. This possibly explains that the largest discrepancy between the mapped τ_{index} obtained with $\tau_{mean\,PIES}$ (1.0560 s) and that produced by $\tau_{mean\,SG}$ (1.0552 s) is found at this station (Figs. 4a and 4c). The amplitude

of the error generated by the original processing method can be reduced by frequent CTD sampling in the study region. However, limited ship time, the loss of some of the array's instruments, and a lack of deep casts in the historical record often prevent an accurate determination of a mean τ field by the PIESs, as exemplified in our case.

b. Baroclinic and absolute current velocity and structure

The use of a single GEM or separate GEMs has little influence on baroclinic volume transport estimates, but it generates notable changes in the current structure, as shown in Fig. 10. The reversal of the current at depths greater than 500 m and surface intensification are better captured when using separate GEMs for the western and eastern regions. When compared with the single-GEM solution $\tau_{mean\,SG}$, the use of two GEMs generally strongly enhances the upper-layer current and reduces the velocities below 200 m on the western half of the array. The opposite is true on the array's eastern half, but to a much lesser extent. The results in Table 2 demonstrate that these changes of the current structure due to the use of separate GEMs reduce significantly the estimate's error. Figure 10 also demonstrates that the PIES-derived baroclinic current structure matches very well that of the Seaglider below $\sim$150–200 m, while the upper-layer current is often underestimated. This underestimation might be caused by the larger error existing across the whole GEMs in the upper layers (this increased error is related to the larger variability in hydrographic properties existing in these layers), which is likely to reduce the amplitude of temperature and specific volume anomaly gradients across the GEM at these depths. This may then explain the slight underestimation of the averaged PIES-derived baroclinic volume transport (14.8 Sv over the periods corresponding to the 15 Seaglider sections) against that obtained by the Seaglider (15.6 Sv).

The improvement in defining the current structure is likely the cause for the improved absolute transport estimates obtained with $\tau_{mean\,SG\,EW}$. While the leveling leads to a significant improvement for $\tau_{mean\,PIES}$ and $\tau_{mean\,Hist}$ in terms of volume transport, optimal results can be reached only through a finer current structure determination. This is exemplified in Fig. 11, which displays the depth-averaged velocity across the array in the upper 400 m (Fig. 11a) and between 400 and 1000 m (Fig. 11b). The velocities determined by the Seaglider are also shown as a reference. For $\tau_{mean\,PIES}$, the leveling leads to a considerable decrease of the volume transport error (7.6 Sv for baroclinic transport vs 4.2 Sv for absolute transport), yet, the velocity time series (blue curves)
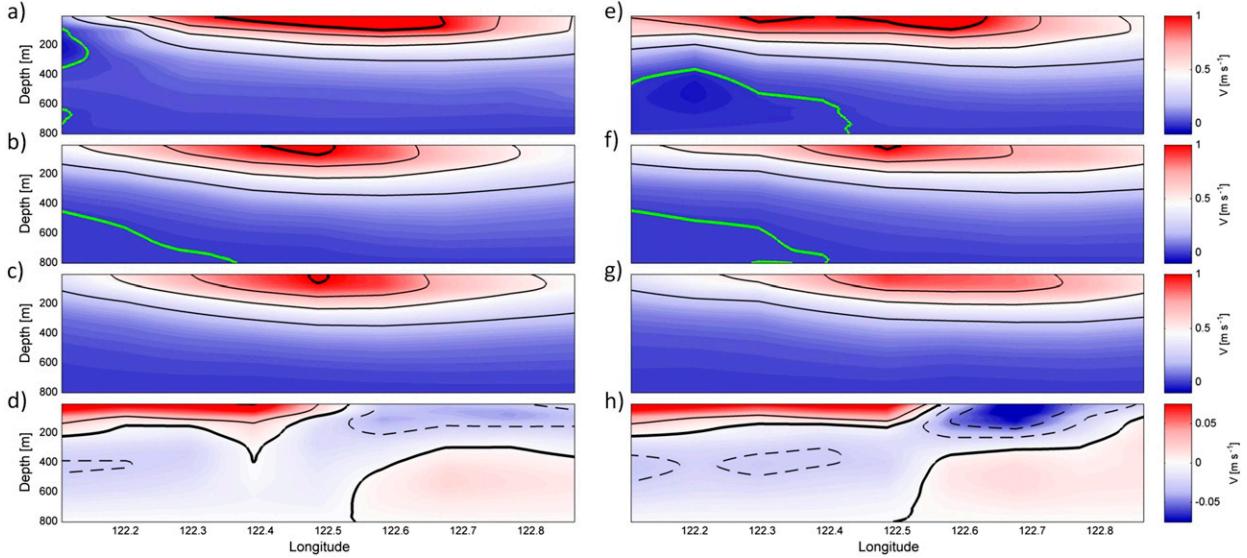
FIG. 10. Baroclinic velocity sections across the PIES array sampled (left) 17–24 Jan 2013 and (right) 12–25 Feb 2013. The velocity data are inferred from measurements by (a),(e) Seaglider; (b),(f) PIES processed with $\tau_{\text{mean SG}}$ and two GEMs; and (c),(g) with $\tau_{\text{mean SG}}$ and a single GEM. (d),(h) Velocity difference between the two-GEM and single-GEM solutions. The level of no motion in all cases is 800 dbar. In the six upper plots, the green (thick black) contour represents the $0\,\text{m s}^{-1}$ ($1\,\text{m s}^{-1}$) isotach and the light contours represent the 0.25, 0.5, and $0.75\,\text{m s}^{-1}$ isotachs. In the two lower panels, thin isotachs indicate intervals of $0.025\,\text{m s}^{-1}$ with solid (dotted) lines for the positive (negative) velocity difference and the thick black line is the $0\,\text{m s}^{-1}$ limit.

of Fig. 11 demonstrate that the current structure is not accurately determined. The current is underestimated in the upper layer and overestimated below 400 m. This pattern is also visible for $\tau_{\text{mean Hist}}$ to a lesser extent. In the case of $\tau_{\text{mean SG}}$, the thermocline depth results (Table 1; Fig. 6) indicate that the hydrography and baroclinic current structure are better rendered than for $\tau_{\text{mean PIES}}$ and $\tau_{\text{mean Hist}}$. But the lower absolute volume transport and velocities of $\tau_{\text{mean SG}}$ (green curves in Figs. 8 and 11) suggest that the absolute velocities are often underestimated at various levels. The results of $\tau_{\text{mean SG EW}}$ however combine an improved definition of the baroclinic current structure and more accurate absolute volume transport and velocities at the upper levels, and in many instances at the lower levels. The marked difference in the absolute velocities of $\tau_{\text{mean SG}}$ and $\tau_{\text{mean SG EW}}$ could arise from the refined determination of the deep hydrography (Fig. 6d) and deep current shear (Figs. 10d and 10h) generated by the use of two GEMs. A better determination of the deep shear should indeed translate into different values in Eq. (9) for the term $(1/T)\sum_{t=0}^{T}\int_{-di}^{-400\text{m}}[\partial(V_{\text{BC}})/\partial z]\,dz$. At each PIES site, this term is always of higher magnitude when using $\tau_{\text{mean SG}}$ than $\tau_{\text{mean SG EW}}$. Concurrently, the term $(1/T)\sum_{t=0}^{T}V(t, 400)$ is also always of lower magnitude than the PIES-integrated shear. The velocity adjustment generated by the leveling process will then reduce the resulting absolute velocities as strongly as the

difference between $1/T\sum_{t=0}^{T}\int_{-di}^{-400\text{m}}[\partial(V_{\text{BC}})/\partial z]\,dz$ and $(1/T)\sum_{t=0}^{T}V(t, 400\,\text{m})$ is large, thus decreasing the transport of $\tau_{\text{mean SG}}$ more than it does for $\tau_{\text{mean SG EW}}$. Last, it appears that most of the contribution for the higher value of the PIES-integrated shear of $\tau_{\text{mean SG}}$ is from the shear below 800 dbar (not shown). We therefore conclude that the improved estimation of the deep hydrography (Fig. 6d) and velocity shear allowed by the use of two separate GEMs is crucial in improving the majority of the absolute velocities estimates.

c. Discrepancies between ADCP- and PIES-derived transports

Though the agreement between ADCP-derived transports and PIES-derived transports is generally excellent, the absolute volume transport results in Fig. 8b display significant discrepancies between the time series obtained from PIES and those from the ADCP during several periods throughout the year of deployment. These discrepancies may arise from the differing nature of the quantities estimated by the ADCP and PIES. The former measures both the geostrophic and ageostrophic components of the current; whereas only the absolute geostrophic current is derived from PIES. Some of the periods of large discrepancies between the two volume transport time series may be associated with the mesoscale eddy–Kuroshio
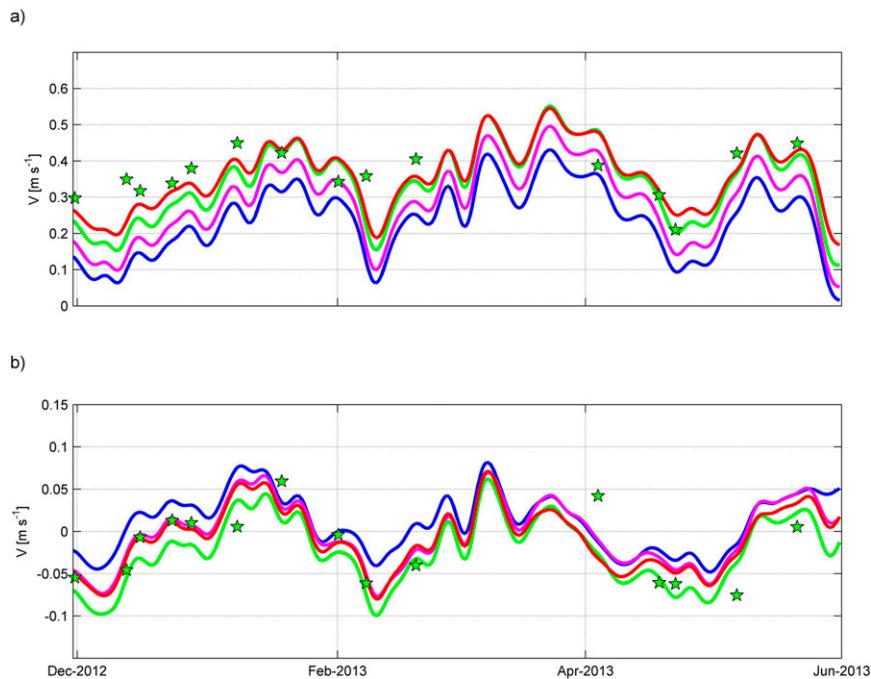
FIG. 11. (a) The 7-day low-pass-filtered time series of depth-averaged current across the PIES array and each Seaglider section, (a) 0–400 dbar and (b) 400–1000 dbar. The color code is identical to that of Figs 8a and 6.

interactions reported in Lien et al. (2014), as in June, July, and December 2012, while some others seem unrelated to such influence (August–September 2012). The detailed analysis of the differences between ADCP- and PIES-derived transports is the subject of an ongoing study.

5. Summary and conclusions

In this paper, we develop modifications to the processing procedure of PIES data that are particularly adapted to environments with 1) water masses having distinct properties that cannot be resolved by an integrated measure like τ, 2) limited hydrographic profiles available for the τ conversion process, and 3) a steep and complex topography. This alternative methodology leads to notable improvements in reproducing the hydrographic and baroclinic structure, as well as baroclinic volume transport across a western boundary current.

The original processing procedure described in Donohue et al. (2010) includes the conversion of the τ measured at the instrument's level to a reference level, τ_{index}. This involves the use of both historical hydrographic data and full-depth hydrographic profiles acquired simultaneously with the PIES measurements.

The τ_{index} is then objectively mapped using a mean field and a residual field. The mean field is obtained from the time averaging of the PIES τ_{index} record. Mapped τ_{index} are then converted to full-depth profiles of temperature and specific volume anomaly using GEM lookup tables.

One of the two main sources of discrepancy associated with this procedure occurs during the conversion of the τ measured by the PIES to the τ_{index} to which GEM lookup tables are referenced. The error of ~0.7 ms reported by Donohue et al. (2010) is likely to be larger if only a limited number of full-depth hydrographic profiles are available for the τ conversion, a situation that is more likely to happen for deep instruments. The error is then propagated during the objective mapping process. We circumvent this problem by replacing the mean τ_{index} field derived from the PIES by a mean field calculated from CTD data. By using a dataset of hydrographic casts captured by two Seagliders sampling simultaneously with the PIES deployments, large improvements are obtained in determining the thermocline depth across the array (37% decrease), baroclinic current shear (22% decrease), and baroclinic velocity and transport (61%). Even when using a τ mean field calculated from a coarsely sampled historical dataset (157 casts in an area of ~180 km × 60 km), significant

improvements can still be achieved. The performance of an historical data–based τ mean field can actually be considerably improved when at least ~20 independent profiles are available around each grid cell; and we recommend PIES users to regularly conduct CTD sampling during the period of PIES observations to reach this figure, preferably with the CTD casts evenly distributed in time.

Another source of errors in the PIES processing stems from the use of a single GEM in those frontal regions where neighboring water masses with very different hydrographic properties generate identical travel times and thus large errors in the GEM lookup tables. In this case, using separate GEMs on each side of the front strongly reduces the GEM rms error, improves the thermocline depth determination, and ensures a more accurate reproduction of the baroclinic current structure. This procedure is particularly relevant along the Kuroshio path, as South China Sea waters interact with the North Pacific waters from the Luzon Strait to the east of Taiwan, the Okinawa trough, and even as far as southern Japan (Chen 2005).

PIES can also provide absolute geostrophic current profiles from the use of its pressure data and measurements of a reference current. The method developed by Andres et al. (2008) is based on the comparison of PIES pressure data, PIES-derived baroclinic velocity, and absolute velocity concurrently measured by a current meter attached to a PIES instrument (CPIES). To estimate the absolute current velocity from PIES, we adapt the aforementioned method for the use of ADCPs instead of a bottom-mounted current meter as a reference for the PIES pressure data. The resulting absolute volume transport time series compare well with those derived from the ADCP with an rms difference of 3.0 Sv. Except for a period of ~90 days near the beginning of the measurements during which the PIES estimates are higher than those of the ADCP, there is little discrepancy between the two time series. The large differences are likely related to the occurrence of ageostrophic processes that have yet to be elucidated.

In summary, the hydrography-based τ mean field will lead to improved estimates if a sufficiently large number of historical hydrographic data are available for the calculation of the mean field, and when there are a limited number of hydrographic casts available for the conversion of τ to τ_{index}. Improvements are also expected in those frontal regions where instrument spacing is large relative to the width of the front and in cases of missing or erroneous τ data at some of an array's sites. In other cases, the original procedure should provide comparable results to the revised procedure.

The use of two separate GEMs is relevant in study regions where different water masses with a similar τ may exist across a front. This procedure leads to an improvement of the deep baroclinic shear, and in turn to absolute velocity estimates. In the case of a temporal ambiguity in interpreting τ (rather than spatial ambiguity), the use of a multi-index GEM procedure (Park et al. 2005) may be more appropriate. In the absence of temporal or spatial τ ambiguity, a single-GEM solution is adequate.

For a dataset such as ours, the τ_{index} processing and leveling methodologies proposed in our study yield better qualitative and quantitative estimates of the hydrography and current velocity, which are essential for the combined study of baroclinic and barotropic currents, and the determination of time-varying current velocity at given reference levels across a western boundary current.

APPENDIX

Determination of an Optimal Barnes Smoothing Length Scale for Generating a Mean τ_{index} Field

The zonal and horizontal smoothing length scales are chosen as a trade-off between limiting the error associated with the interpolation of τ_{index} within each gridded cell, which is obtained with small smoothing scales, and benefiting from a large spatial correlation between each cell, which is attained with large smoothing scales. For this purpose, we establish the ϵ index, which takes into account these two parameters, as follows:

$$\epsilon_{(xr,yr)} = \frac{1}{N} \sum \frac{\varsigma\{\tau_{\text{index}}[x(i)]\}}{\gamma_{|xr,yr}}.$$

Here, xr and yr represent the zonal and meridional length scales, respectively; $x(i)$ refers to each grid cell between H1 and H4; and $N = 1, 2, \ldots, i$, to the number of cells along the latitude of interest (18.75°N). The numerator ς expresses the interpolation error, and the denominator γ represents the magnitude of smoothing. These terms are obtained as follows:

The term ς is a quantity calculated at each grid cell, being the standard deviation of the τ_{index} derived from every casts included within xr, yr. This standard deviation is weighted by the Barnes interpolation weighting coefficients.

The term γ is obtained after determination of the gridded τ_{index} values. We first calculate the standard deviation of the gridded τ_{index} along 18.75°N obtained through the Barnes scheme at a given xr and yr: $\tau_{\text{index}}(x)_{\text{barnes}}$.

We also calculate the standard deviation of the gridded τ_{index} obtained via a classic averaging of all τ_{index} included within the 10-km-sided cells: $\tau_{\text{index}}(x)_{\text{mean}}$, γ is the ratio of the former on the latter, and

$$\gamma_{|xr,yr} = \frac{\sigma[\tau_{\text{index}}(x)]_{\text{barnes}|xr,yr}}{\sigma[\tau_{\text{index}}(x)]_{\text{mean}}};$$

hence, the larger the smoothing scale is, the smaller the ratio becomes.

Therefore, both γ and ς decrease for larger smoothing scales, but they do so unequally, and the optimum pair of (xr, yr) is the one that minimizes ϵ. For $\tau_{\text{mean SG}}$, we obtain $xr = 0.30°$ and $yr = 0.22°$, whereas for $\tau_{\text{mean Hist}}$, $xr = 0.14°$ and $yr = 0.30°$. This difference may be explained by the data density and distribution of the two fields. For $\tau_{\text{mean SG}}$, more data are available zonally than meridionally (Fig. 1), and the best trade-off between error and smoothing is found at relatively larger zonal scales. Conversely, for $\tau_{\text{mean Hist}}$ the data density in both zonal and meridional directions is equally low. This shortcoming may be compensated by the coherence of hydrography properties along the Kuroshio flow, leading to a larger meridional than zonal smoothing scale.

The use of these figures yields better (thermocline depth, baroclinic, and absolute transport) estimations than arbitrarily chosen smoothing length scales. Testing shows however that using smoothing length scales of $xr = 0.15°$ and $yr = 0.15°$—that is, one and a half times the grid spacing—generates volume transports estimates within 0.5 Sv of those shown in this study.

REFERENCES

Andres, M., M. Wimbush, J.-H. Park, K.-I. Chang, B.-H. Lim, D. R. Watts, H. Ichikawa, and W. J. Teague, 2008: Observations of Kuroshio flow variations in the East China Sea. *J. Geophys. Res.*, **113**, C05013, doi:10.1029/2007JC004200.

Barnes, S. L., 1964: A technique for maximizing details in a numerical weather map analysis. *J. Appl. Meteor.*, **3**, 396–409, doi:10.1175/1520-0450(1964)003<0396:ATFMDI>2.0.CO;2.

Book, J., M. Wimbush, S. Imawaki, H. Ichikawa, H. Uchida, and H. Kinoshita, 2002: Kuroshio temporal and spatial variations south of Japan, determined from inverted echo sounder measurements. *J. Geophys. Res.*, **107**, 3121, doi:10.1029/2001JC000795.

Bretherton, F. P., R. E. Davis, and C. B. Fandry, 1976: A technique for objective analysis and design of oceanographic experiments applied to MODE-73. *Deep-Sea Res. Oceanogr. Abstr.*, **23**, 559–582, doi:10.1016/0011-7471(76)90001-2.

Chen, C.-T. A., 2005: Tracing tropical and intermediate waters from the South China Sea to the Okinawa Trough and beyond. *J. Geophys. Res.*, **110**, C05012, doi:10.1029/2004JC002494.

——, and S.-L. Wang, 1998: Influence of intermediate water in the western Okinawa Trough by the outflow from the South China Sea. *J. Geophys. Res.*, **103**, 12 683–12 688, doi:10.1029/98JC00366.

Donohue, K. A., D. R. Watts, K. L. Tracey, A. D. Greene, and M. Kennelly, 2010: Mapping circulation in the Kuroshio Extension with an array of current and pressure recording inverted echo sounders. *J. Atmos. Oceanic Technol.*, **27**, 507–527, doi:10.1175/2009JTECHO686.1.

Jan, S., and Coauthors, 2015: Large variability of the Kuroshio at 23.75°N east of Taiwan. *J. Geophys. Res. Oceans*, **120**, 1825–1840, doi:10.1002/2014JC010614.

Kennelly, M., K. L. Tracey, and D. R. Watts, 2007: Inverted echo sounder data processing manual. GSO Tech. Rep. 2007–02, Graduate School of Oceanography, University of Rhode Island, 87 pp.

Lien, R.-C., B. Ma, Y.-H. Cheng, C.-R. Ho, B. Qiu, C. M. Lee, and M.-H. Chang, 2014: Modulation of Kuroshio transport by mesoscale eddies at the Luzon Strait entrance. *J. Geophys. Res. Oceans*, **119**, 2129–2142, doi:10.1002/2013JC009548.

——, and Coauthors, 2015: The Kuroshio and Luzon Undercurrent east of Luzon Island. *Oceanography*, **28** (4), 54–63, doi:10.5670/oceanog.2015.81.

Meinen, C. S., and D. R. Watts, 2000: Vertical structure and transport on a transect across the North Atlantic Current near 42°N: Time series and mean. *J. Geophys. Res.*, **105**, 21 869–21 891, doi:10.1029/2000JC900097.

Mensah, V., S. Jan, M.-D. Chiou, T.-H. Kuo, and R.-C. Lien, 2014: Evolution of the Kuroshio Tropical Water from the Luzon Strait to the east of Taiwan. *Deep-Sea Res. I*, **86**, 68–81, doi:10.1016/j.dsr.2014.01.005.

——, ——, M.-H. Chang, and Y.-J. Yang, 2015: Intraseasonal to seasonal variability of the intermediate waters along the Kuroshio path east of Taiwan. *J. Geophys. Res. Oceans*, **120**, 5473–5489, doi:10.1002/2015JC010768.

Park, J.-H., D. R. Watts, and K. L. Tracey, 2005: A multi-index GEM technique and its application to the southwestern Japan/East Sea. *J. Atmos. Oceanic Technol.*, **22**, 1282–1293, doi:10.1175/JTECH1778.1.

Sun, C., and D. R. Watts, 2001: A circumpolar gravest empirical mode for the Southern Ocean hydrography. *J. Geophys. Res.*, **106**, 2833–2855, doi:10.1029/2000JC900112.

Todd, R. E., D. L. Rudnick, M. R. Mazloff, R. E. Davis, and B. D. Cornuelle, 2011: Poleward flows in the southern California Current System: Glider observations and numerical simulation. *J. Geophys. Res.*, **116**, C02026, doi:10.1029/2010JC006536.

Tracey, K. L., and D. R. Watts, 1986: On Gulf Stream meander characteristics near Cape Hatteras. *J. Geophys. Res.*, **91**, 7587–7602, doi:10.1029/JC091iC06p07587.

Tsai, C.-J., M. Andres, S. Jan, V. Mensah, T. B. Sanford, R.-C. Lien, and C. M. Lee, 2015: Eddy-Kuroshio interaction processes revealed by mooring observations off Taiwan and Luzon. *Geophys. Res. Lett.*, **42**, 8098–8105, doi:10.1002/2015GL065814.

Watts, D. R., and H. T. Rossby, 1977: Measuring dynamic heights with inverted echo sounders: Results from MODE. *J. Phys. Oceanogr.*, **7**, 345–358, doi:10.1175/1520-0485(1977)007<0345:MDHWIE>2.0.CO;2.

——, C. Sun, and S. Rintoul, 2001: Two-dimensional gravest empirical modes determined from hydrographic observations in the Subantarctic Front. *J. Phys. Oceanogr.*, **31**, 2186–2209, doi:10.1175/1520-0485(2001)031<2186:ATDGEM>2.0.CO;2.